JOURNAL OF SOLID STATE CHEMISTRY **131,** 215–220 (1997)
ARTICLE NO. SC977357

Evidence of Translational Disorder Generated by Oriented Defects in Magneli Phases

L. Sangaletti, L. E. Depero, E. Bontempi, R. Salari, and G. Sberveglieri

Istituto Nazionale per la Fisica della Materia and Dipartimento di Chimica e Fisica per i Materiali, Università di Brescia, Via Branze, 38, 25123 Brescia, Italy

Received August 23, 1996; in revised form January 31, 1997; accepted February 18, 1997

Structural modeling and simulations are proposed to justify the X-ray diffraction pattern of oxygen-deficient Ti : WO_3 thin films, where the lack of 2-D and 3-D correlations observed in the structure is ascribed to a random spacing between {1 0 3} crystallographic shear planes while maintaining the defect density of the $WO_{2.9}$ ordered structure. The present phase can be viewed as an intermediate case between the crystalline and the amorphous WO_3 phases, due to the freezing of the in-plane rotational degree of freedom of the $[WO_6]^{6-}$ structural unit. © 1997 Academic Press

Tungsten trioxide, WO_3, shows a remarkable variety of physical properties which can be ultimately related to the microstructural properties. The amorphous phase is required to obtain electrochromism (1). Oxygen-deficient tungsten trioxide (WO_{3-x}) is known to crystallize in the Magneli phases, which offer a wide range of structures originated by the presence of ordered patterns of edge-sharing $[WO_6]^{6-}$ octahedra within the ReO_3-like corner-sharing octahedra network (2–12). WO_3 is also antiferroelectric and, in the closely related WO_3-based tungsten bronzes, superconductivity and electrochromism are found, depending on the degree of doping (13). In addition, pure WO_3 and Ti–W–O mixed oxides have been recently produced in the form of thin films and are currently being tested as gas sensors (14–16).

As for the microstructural properties, it should be noticed that structures discovered in the bulk (single crystals or powders) might not properly describe those of thin film materials (17) or nanopowders (18). Furthermore, metastable phases are likely to be found in thin films (19–21), in view of the out-of-equilibrium growing conditions and of the stresses induced by the substrate at the interface. Also for the present material, i.e., oxygen–deficient Ti : WO_3 thin films deposited by r.f. sputtering, structural modeling and simulations have been formulated to justify the X-ray diffraction (XRD) patterns which could not be directly related to those of the bulk phase. The lack of 2-D and 3-D correlations observed in the XRD pattern is ascribed to the disorder effect of the $WO_{2.9}$ structure due to a random spacing between {1 0 3} crystallographic shear planes. In this frame, the experimental results and their interpretation bring evidence of translational disorder generated by oriented defects in the WO_3 Magneli phases. The present phase can be regarded as an intermediate case between the crystalline and the amorphous WO_3 phases, due to the freezing of the in-plane rotational degree of freedom of the $[WO_6]^{6-}$ structural unit (considered a rigid body).

Ti–WO_3 thin films were deposited onto alumina substrates by r.f. magnetron sputtering from a target of the Ti–W alloy (90% W–10% Ti in atomic weight) by using an Alcatel (Model 450 SCM) sputtering plant. The use of titanium in the Ti–W target alloy was aimed to improve the thin film adhesion properties. The pressure inside the chamber was 0.0125 mbar and four samples with different Ar/O_2 ratios, i.e., 20, 30, 40, and 60% O_2 content in the gas mixture, were grown. X-ray diffraction measurements were performed on a Philips MPD 1830 powder diffractometer with graphite monochromated Cu$K\alpha$ radiation in the Bragg–Brentano parafocusing geometry. Simulations and modeling were performed by the Cerius^2 software package (22).

Despite the considerable amount of Ti atoms in the target ($\approx 40\%$ of the atoms in the target are Ti atoms), the as-grown samples usually show a lower Ti/W atomic ratio, which increases with annealing treatments (16). Therefore, in the present samples titanium is regarded as an impurity for the WO_x lattice. The effect of Ti cations on the WO_x lattice has been discussed in a recent study (16). These defects can be ascribed to the tendency of Ti atoms to form edge-sharing Ti–O octahedra which can originate disorder in the network of the W–O corner-sharing octahedra characteristic of WO_3. However, despite the lower Ti sputtering rate, the amount of Ti is still relevant and the presence of poorly crystallized or amorphous Ti–O phases may not, in principle, be excluded.

As for the present samples, Ti–O segregated phases are excluded, within the instrumental sensitivity, on the basis of an optical and micro-Raman investigation. Indeed,

0022-4596/97 $25.00

a micro-Raman mapping (with a spatial resolution of about 1 μm) of the layers did not show any phase inhomogeneity. This result was also confirmed by an analysis with an optical microscope. The optical inspection is, in the present case, indicative of sample inhomogeneity since previous studies (21, 23) have shown that phase segregation is related to modification of the layer morphology on a micrometer scale. For example, 0.5–5.0 μm sized WO_3 crystallites were found over the sample surface after annealing for several hours at high temperatures and the area around the crystallites appeared to be Ti rich (from EDS analysis). The signal from WO_3 crystallites was easily detected by XRD. For annealing treatments of about 8 h at 800°C, segregation of nanophase TiO_2 anatase was found by TEM measurements. The signal from TiO_2 anatase was also easily detected by micro-Raman measurements. Moreover, samples with a high Ti content on the surface showed a brown color. This is not the case of the present samples which were not annealed after the deposition and do not show any of the features mentioned above. Therefore they are assumed to be homogeneous within the sensitivity of the micro-Raman probe.

Figure 1 shows the XRD pattern of the Ti–W–O thin films. The Al_2O_3 reflections from the substrate are identified through the bar sequence on the top of the figure. As shown by the intensity trend of the Al_2O_3 reflections, the substrate signal increases with the oxygen content in the mixture, which can be ascribed to a less efficient sputtering process. The thin film contribution to the XRD pattern is given by several structures. First, the strong 001 and 002 reflections are detected at 24° and 46° (2θ). These peaks are relatively narrow with respect to the "amorphous-like" structures detectable in the pattern at 25°, 50°–54°, and 76°. Moreover, the sharp structures are found at scattering angles different from the amorphous maximum, which indicates that the distance corresponding to the sharp peak is slightly different from the average W–W distance in the ReO_3-related structures of WO_3. The presence of amorphous-like structures at high scattering angles (50°–54°, and 76°) is quite unusual. It should also be observed that the lattice spacing corresponding to these reflections are multiple of $\sim$3.5 Å, the average W–W distance, d_{AVE}, in the corner-sharing bonding of the $[WO_6]^{6-}$ octahedra. Furthermore, while in the case of the sharp reflections the third order is not detectable, in the case of the broad reflections the third order can be found peaked at 76°. Finally, the intensities of the broad peaks decrease with the scattering angle. The lack of *hkl* reflections with at least two nonzero indexes is another important finding, which indicates the lack of structural correlation both in two and three dimensions.

The features described so far are more clearly detectable in the sample deposited with the lowest O_2 content and, therefore, the possible structural models have been related to oxygen-deficient WO_{3-x} phases. When an anion deficiency is introduced in the structure, the anion vacancies can be eliminated by sharing one part of the structure relative to the other along a certain crystallographic direction. This defect is, however, observed in a narrow range of oxygen stoichiometries (WO_{3-x} with $0 < x \leqslant 0.13$).

The crystallographic shear (*CS*) phases can be regarded as translational modulations of the parent structure, the translation boundaries being *CS* planes. In particular, oxygen

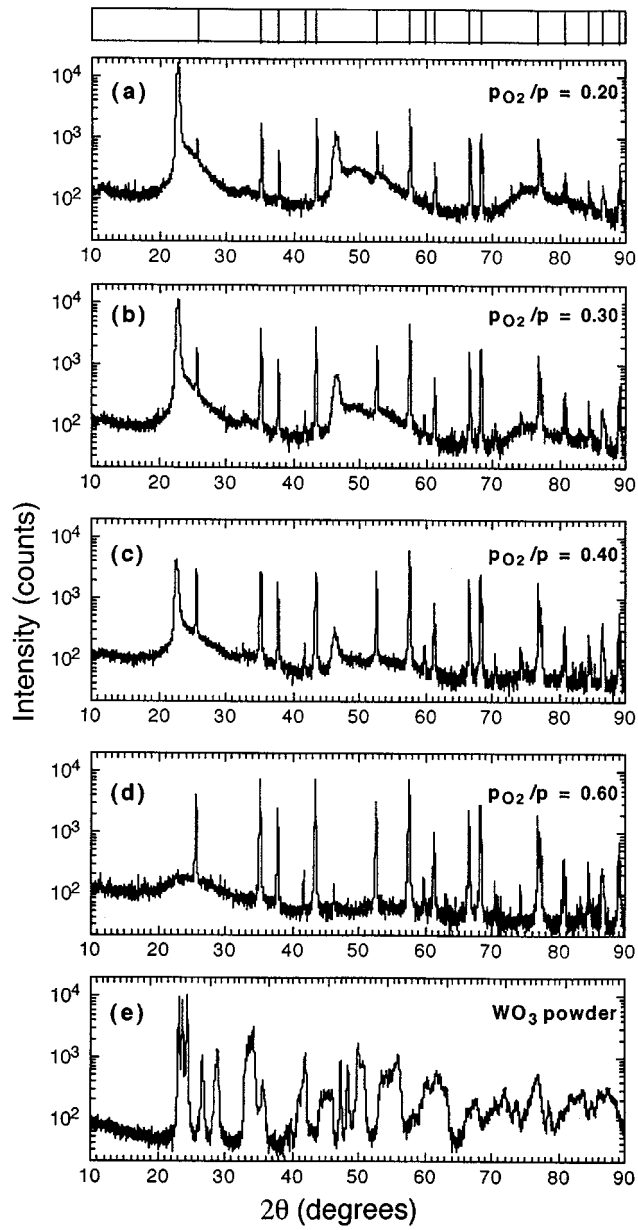

FIG. 1. XRD patterns of samples grown with 20% (a), 30% (b), 40% (c), and 60% (d) O_2 content in the gas mixture. As references, the 2θ position of the Al_2O_3 pattern (top) and the XRD pattern of pure WO_3 powder (e) are reported. A logarithmic scale is used to enhance the "disorder" contribution to the pattern.

removal causes the WO_3 structure to collapse along the {102} planes, thereby introducing {102} *CS* planes into the crystal. The idealized structure of these defects consists of blocks of four edge-shared octahedra in a normal ReO_3-type of structure. Below about $WO_{2.93}$, {103} *CS* planes are introduced in the structure, resulting in blocks of six edge-sharing octahedra (see, e.g., K. Kosuge in Ref. 2). While, in the former cases, the octahedra edges in the plane remain parallel to each other, other phases are known with lower oxygen content where also a rotation of the octahedra with respect to each other is present (see, e.g., $WO_{2.8}$, $WO_{2.76}$, $WO_{2.72}$, $WO_{2.625}$ (24)).

All the WO_{3-x} structures share a common feature. Namely, the measure of one cell parameter corresponds to the height of a $[WO_6]^{6-}$ octahedron, while in the plane perpendicular to this axis, defects can be found according to the oxygen content. When these defects are due to *CS* ordered planes, the Magneli phases may occur.

In view of these common features reported for WO_{3-x}, a model is proposed for the present layers, based on oxygen-deficient layers orderly stacking in one direction. In this way, the sharp reflections detected at 22.8° and 47.5° are ascribed to the constant interlayer spacing, while the broad features detected in the pattern are related to disorder effects within each layer and, in particular, to the average in-plane nearest-neighbor W–W distance d_{AVE}. Actually, a similar feature is also found in the XRD pattern of the amorphous phase, but the presence of these features even at high scattering angles indicates that, despite disorder effects, a monodimensional correlation is present. The difference between the amorphous and the present phase can be ascribed to the orientation of the $[WO_6]^{6-}$ octahedra. While in the amorphous case the octahedra are randomly oriented, in the present phase disorder is supposed to result only from the sliding and not from the rotation of the octahedra. This sliding, which is related to the edge-sharing defects observed in the oxygen-deficient phases of WO_3, can still maintain a correlation of the atomic distributions. In this frame, the present phase can be viewed as an intermediate case between the crystalline and the amorphous, in that, while the octahedron (considered as a rigid body) has zero in-plane degrees of freedom in the crystalline phase and three in the amorphous phase, only the two translational in-plane degrees of freedom are found for the present layer.

The broad halo detected in the 44°–57° range shows, to a close inspection, some structure. Indeed, two maxima are clearly observed at 50° and 54° in the experimental pattern (Fig. 2), which indicates that different average periodicity — due to different sequence of defects in the two orthogonal directions — may be found. The defects in the plane can be related to an increase in the number of edge-sharing octahedra which pack in the plane with respect to the ideal ReO_3-like plane. The presence of these two maxima allowed estimation of the oxygen stoichiometry in the sample. The

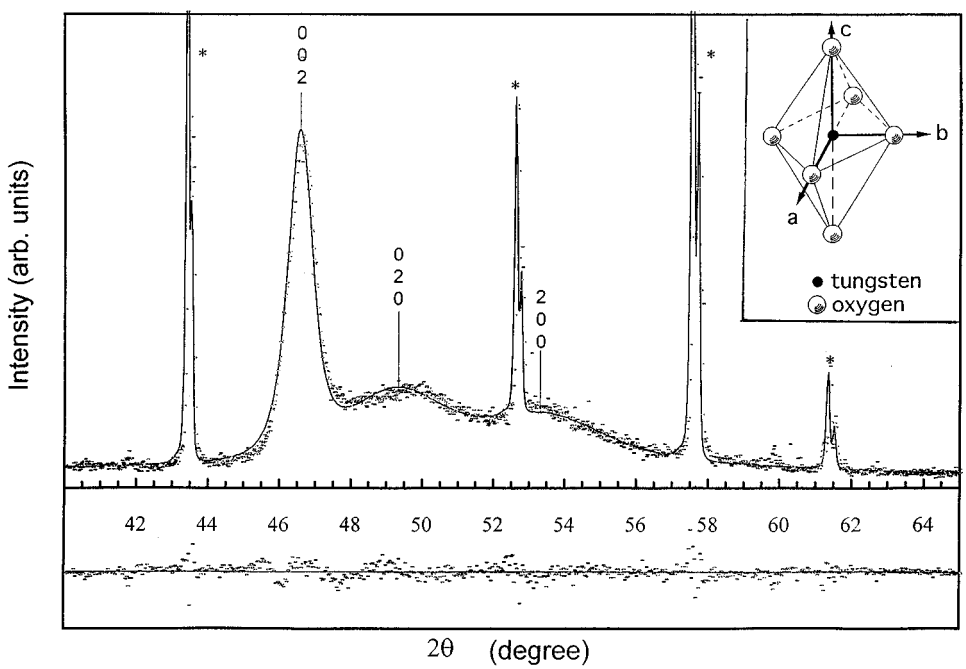

FIG. 2. Expanded view of the pattern shown in Fig. 1a. The data fitting is drawn with a continuous line. On the bottom, the difference between the experimental and the calculated data is reported. The Al_2O_3 reflections are indicated with asterisks. The inset shows the $[WO_6]^{6-}$ octahedral unit and the three axes, *a*, *b*, and *c*, corresponding to the body diagonals.

peak positions have been determined by fitting the experimental data with the PC-APD software package (Fig. 2). The $h00$, $0k0$, and $00l$ reflections detected in the experimental pattern correspond, in the WO_3 structure, to the directions identified by the octahedron diagonals. On the basis of the oxygen-deficient $WO_{2.9}$ structure reported in literature (ICSD Card No. 24736, Ref. 24) showing a {103} *CS* defect, a supercell has been generated to allow a comparison with the ideal WO_3 structure (ICSD Card No. 836, Ref. 24] based on the axis transformation described by the matrix

$$\begin{matrix} 5 & 0 & 6 \\ 0 & 1 & 0 \\ -11 & 0 & 2. \end{matrix}$$

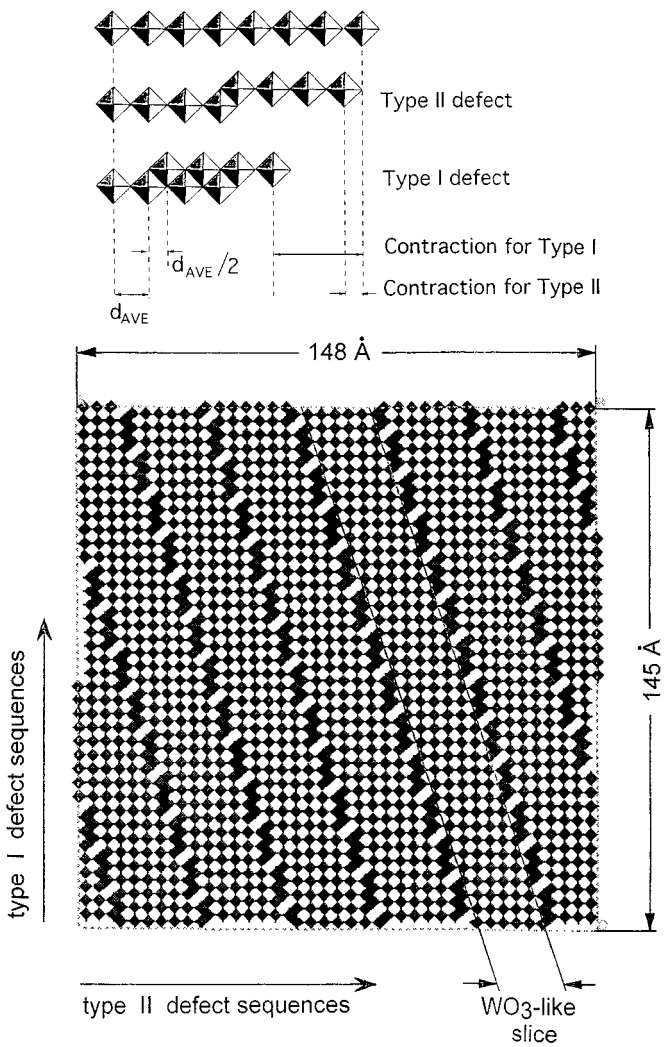

FIG. 3. Supercell, obtained by proper matrix transformation, for the $WO_{2.9}$ phase. A total of 41 octahedra are found in the type I defect sequence direction, while 43 octahedra are found along the type II defect direction.

The presence of one defect in the $WO_{2.9}$ structure was related to a contraction of 1/2 of the W–W distance (Fig. 3). The counting was performed along the directions corresponding to the corner-sharing octahedra rows in the ideal WO_3 structure, with a reference unit length corresponding to the in-plane W–W (d_{AVE}) distance, as shown in Fig. 3. The calculated contractions are reported in Table 1. The calculated Ti–W–O parameters have been obtained starting from the experimental value of the *c*-axis (7.808 Å) and scaling the other two axis lengths according to the ideal WO_3 structure. On the basis of these data, the oxygen content can be estimated and the oxygen stoichiometry of the present sample results to be very close to 2.9. It is remarkable to observe that despite disorder, different contractions are maintained along the two directions, which can be related to the characteristic shape of the defect, as described above.

Another important feature concerns the relative intensity of the reflections belonging to the same family in the experimental pattern. While the measured intensity for the 002 and 004 reflections agrees with the expected intensities in the case of the ordered structure along the corresponding direction, i.e., the *c*-axis (see Fig. 1), for the other detected reflections the intensity ratio between reflections of the same family is different from that observed in the ordered structure. This effect has been simulated by introducing disorder effects into a monodimensional chain of 50 W atoms.

The calculated contribution to the XRD pattern from the two possible defect clusters (I and II) each distributed along one direction with the same density as that found in $WO_{2.9}$ is shown in Fig. 4. The calculation was performed according to the procedure suggested by Warren (25),

$$\frac{I}{I_0} = N_u + \sum_i n_i \frac{\sin(kd_i)}{kd_i},$$

where N_u is the number (50) of scattering units, d_i are the possible W–W distances (multiple of $a/2$) for a given

TABLE 1

Projected W–W Average Distance, d_{AVE} (in Å), along Three Orthogonal Axes for WO_3, Ti–WO_3 (as Obtained from the XRD Data of Fig. 2), and Ti : WO_3 Normalized with Respect to the WO_3 Cell Parameters. Ratio between the Experimental and Calculated d_{AVE} Distances for Ti : WO_3. Ratio between the d_{AVE} Distances of $WO_{2.9}$ and WO_3

Axis	WO_3	Ti : WO_3 experimental	Ti : WO_3 calculated (i.e., normalized to WO_3)	Ti : WO_3 exp/calc	$WO_{2.9}/WO_3$
c	3.877	3.904	3.904	1	1
a	3.785	3.699	3.811	0.971	0.974
b	3.670	3.428	3.696	0.927	0.927

Note. The orthogonal axis corresponds to the body diagonal of the $[WO_6]^{6-}$ octahedron (see inset of Fig. 2).

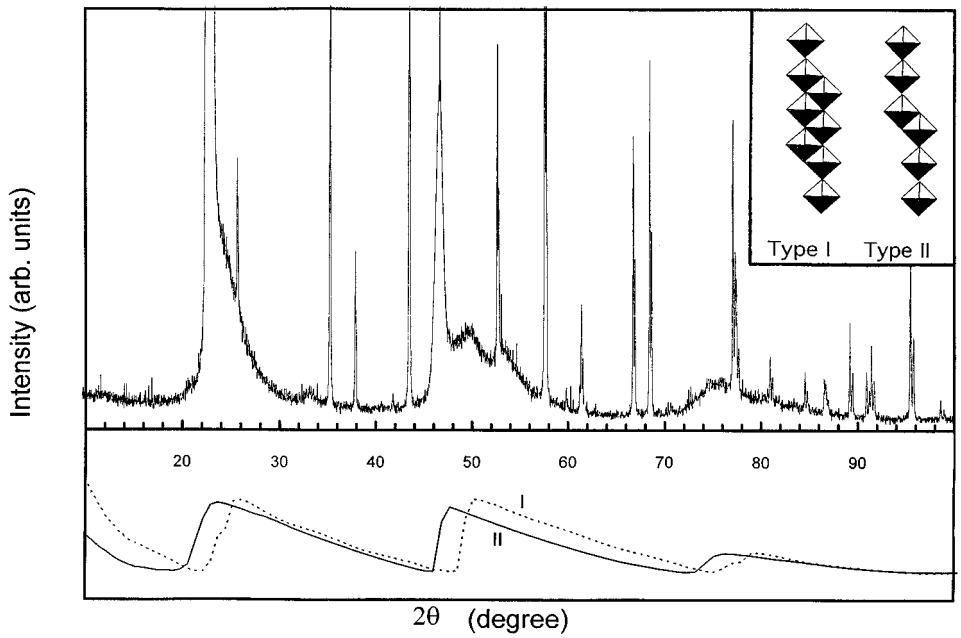

FIG. 4. XRD pattern of the sample grown with 20% O_2 content in the gas mixture compared with the pattern calculated on the basis of the structural simulation. Inset: the two sequences of defects (type I and type II) used in the simulation.

distribution, n_i is the total number of the d_i distances, and $k = 4\pi \sin\theta/\lambda$ ($\lambda = 1.541$ Å, Cu$K\alpha$). The simulated pattern is in good agreement with both integrated intensity and the peak positions. In particular, the proposed model shows that the defect clusters I, originated by the $\{1\,0\,3\}$ *CS*, are oriented parallel to each other. Indeed, as can be evinced by a close inspection of Fig. 3, this orientation implies that the defect distribution along two orthogonal directions is different.

In conclusion, the XRD patterns and the structural modeling bring evidence of translational disorder generated by oriented defects in the Magneli phases. The lack of correlation in the structure can be ascribed to a random spacing between $\{1\,0\,3\}$ planes while keeping the defect density and therefore the axis correlations of the $WO_{2.9}$ ordered structure. This kind of translational disorder may affect the electrochromic properties of this material. Indeed, a change in the thin film color (from green–gray to pale yellow) was observed with the increase in oxygen in the Ar/O_2 gas mixture.

REFERENCES

1. K. Bange and T. Gambke, *Adv. Mater.* **1,** 10 (1990).
2. Detailed and comprehensive descriptions of the mechanisms of shear structure formation can be found in, e.g., A. D. Wadsley and S. Andersson, *in* "Perspectives in Structural Chemistry" (J. D. Dunitz and J. A. Ibers, Eds.), Vol. 3, Chap. 1. Wiley, New York, 1970; B. G. Hyde and S. Andersson, "Inorganic Crystal Structures." Wiley, New York, 1989; R. J. D. Tilley, "Defect Crystal Chemistry." Blackie, Glasgow, 1987; K. Kosuge, "Chemistry of Nonstoichiometric Compounds." Chap. 2. Oxford Univ. Press, Oxford, 1994.
3. M. Sundberg, *Acta Crystallogr. B* **32,** 2144 (1976).
4. I. J. McColm, R. Steadman, and S. J. Wilson, *J. Solid State Chem.* **23,** 33 (1978).
5. A. Magnéli, *Arkiv Kemi* **1,** 223 (1949).
6. A. Magnéli, *Arkiv Kemi* **1,** 513 (1949).
7. A. Magnéli, *Acta Crystallogr.* **6,** 495 (1953).
8. M. M. Dobson and R. J. D. Tilley, *Acta Crystallogr. B* **44,** 474 (1988).
9. Y. A. Barabenenkov, N. D. Zakharov, I. P. Zibrov, V. P. Filonenko, P. Werner, A. I. Popov, and M. D. Valkovskii, *Acta Crystallogr. B* **49,** 169 (1993).
10. M. Sundberg, N. D. Zakharov, I. P. Zibrov, Y. A. Barabenenkov, V. P. Filonenko, and P. Werner, *Acta Crystallogr. B* **49,** 951 (1993).
11. R. Pickering and R. J. D. Tilley, *J. Solid State Chem.* **16,** 247 (1976).
12. S. Iijima, *J. Solid State Chem.* **14,** 52 (1974).
13. N. Tsuda, K. Nasu, A. Yanase, and K. Siratori, "Electronic Conduction in Oxides," Chap. 4. Springer-Verlag, Berlin, 1991.
14. L. E. Depero, I. Natali Sora, C. Perego, L. Sangaletti, and G. Sberveglieri, *Sensors Actuators B* **31,** 19 (1996).
15. P. Nelli, L. E. Depero, S. Groppelli, F. Ronconi, L. Sangaletti, and G. Sberveglieri *Sensors Actuators B* **31,** 89 (1996).
16. L. E. Depero, S. Groppelli, I. Natali Soda, L. Sangaletti, G. Sberveglieri, and E. Tondello, *J. Solid State Chem.* **121,** 379 (1996).
17. L. Sangaletti, L. E. Depero, and L. Armelao, "Material Science Forum, Proceedings of the Fourth European Powder Diffraction Conference, EPDIC IV, Chester (UK), July, 1995."
18. L. E. Depero and P. Levrangi, *J. Solid State Chem.* **110,** 190 (1994).
19. L. E. Depero, L. Sangaletti, C. Schaffinit, F. Rossi, and P. N. Gibson, *in* "Covalent Ceramics III-Science and Technology of Non-Oxides" (G. S. Fishman, A. E. Hepp, P. N. Kumta, A. E. Kaloyeros, and J. J. Sullivan, Eds.), Symposium Proceedings Series. Vol. 410. Materials Research Society, Pittsburgh, 1996.
20. L. E. Depero, C. Perego, L. Sangaletti, and G. Sberveglieri, *in* "Polycrystalline Thin Films: Structure, Texture, Properties and Applications II" (H. J. Frost, C. A. Ross, M. A. Parker, and E. A. Holm, Eds.), Symposium Proceedings Series. Vol. 403. Materials Research Society, Pittsburgh, 1996.

21. G. Sberveglieri, L. E. Depero, M. Ferroni, V. Guidi, G. Martinelli, P. Nelli, C. Perego, and L. Sangaletti, *Adv. Mater.* **8,** 334 (1996).
22. The Cerius^2 1.6 software is released by Molecular Simulations Inc.
23. L. Sangaletti, E. Bontempi, L. E. Depero, P. Galinetto, S. Groppelli, R. Salari, and G. Sberveglieri, *in* "Thin Films: Surface and Morphology" (R. Cammarata, E. Chason, Th. Einstein, and E. Williams, Eds.), Symposium Proceedings Series, Vol. 441. Materials Research Society, Pittsburgh, 1997.
24. Inorganic Crystal Structure Database, ICSD, Gmel-Institut Für anorgranische Chemie and Fachinformazionszentrum FIZ Karlsruhe, Release 1995.
25. B. E. Warren, "X-Ray Differentiation," Chap. 10. Dover, New York, 1990.